

Revisiting Selenium Interactions with Pyrite: From Adsorption to Coprecipitation

Carolina Guida,[○] Vivien Ramothe,[○] Anthony Chappaz,* Pauline Simonnin, Kevin M. Rosso, Rong-Rong Ding, Damien Prieur, Andreas C. Scheinost, and Laurent Charlet*



Cite This: *ACS Earth Space Chem.* 2024, 8, 67–78



Read Online

ACCESS |

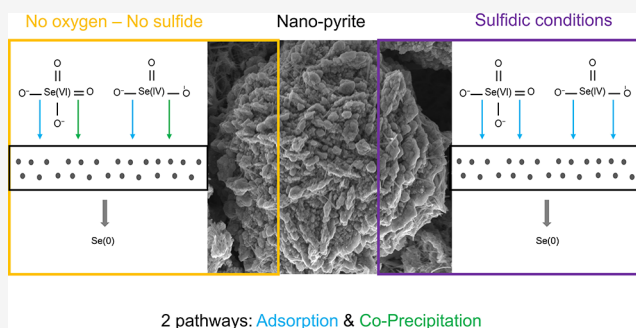
Metrics & More

Article Recommendations

Supporting Information

ABSTRACT: Interactions of selenium (Se), a trace element bioessential at low concentrations but highly toxic at high concentrations, with the most abundant sulfide mineral in the earth's crust, namely, pyrite, were investigated over a wide range of time scales from nanoseconds to days. At the nanosecond scale, selenate Se(VI)O_4^{2-} adsorption onto the neat pyrite surface is shown by *ab initio* computations to proceed via the formation of a chemical bond between an oxyanion oxygen atom and a surface Fe atom, weakening the other Se–O bonds and reducing the Se atom oxidation state. At the hour-to-day scale, the adsorption and coprecipitation of selenate Se(VI)O_4^{2-} and selenite, Se(IV)O_3^{2-} , were investigated through wet chemical batch experiments at various pH values at different sulfide concentrations. Selenium removal from solution is slower and weaker for selenate than for selenite. After 24 h, only 10% of selenate, against 60% of selenite (up to 100% in the presence of sulfide), is removed by the pyrite surface. Independently of its original oxidation state, adsorbed Se is completely reduced to elemental trigonal selenium via adsorption, precipitation, or coprecipitation, as shown by XANES spectroscopy. Our EXAFS results, compared to published data on Se-rich pyrite, show a Se to S substitution within the pyrite structure. The reductive coprecipitation mechanism of selenium with pyrite represents valuable new insights for improving our understanding of modern and ancient biogeochemical cycles involving Se. In addition, several industries can benefit from direct applications of our findings, such as water treatment, green technologies, and sustainable mining.

KEYWORDS: selenium, pyrite, adsorption, coprecipitation, theoretical calculations, XANES



INTRODUCTION

Positioned underneath sulfur (S) in the periodic table, selenium (Se), a redox-sensitive metalloid, shares features similar to those of this major element. Like S, it is enriched in geological settings buried under anoxic conditions (shales, coal¹) and displays a wide range of oxidation states ranging from –II to +VI with Se(–II), Se(–I), Se(0), Se(IV), and Se(VI) being the most predominant under natural conditions.^{1,2} In aquatic systems, Se(IV) and Se(VI) species are usually dissolved, while Se(0), Se(–I), and Se(–II) in the presence of iron minerals exhibit low solubilities.^{3,4} The use of Se as a paleo-redox proxy has been considered because of its different oxidation states and the occurrence of several stable isotopes in the environment.⁵ The annual average production of Se is ~3355 tons.⁹ The main application is in metallurgy for producing electrolytic manganese as an additive in the steel manufacturing industry. Selenium is an essential nutrient fulfilling biological functions that cannot be substituted by other elements. It is also used in the agricultural, food, and pharmaceutical industries as an additive, fertilizer, dietary supplement, and fungicide to control dermatitis.⁹ Some plants

can uptake and metabolize Se as the ion selenate via sulfate transporters.⁶ For humans, the required Se intake is between 50 and 400 $\mu\text{g}/\text{day}$.⁷ Se represents a bioessential trace element involved in the enzyme glutathione peroxidase that converts peroxide into water and catalyzes the scavenging of free radicals, preventing oxidative damage to biological tissues.^{8,9} However, Se can induce severe toxic effects on aquatic life at an intake reaching 800 $\mu\text{g}/\text{day}$,⁷ causing deformities, a lower reproduction rate, and higher mortality.¹⁰

The main natural sources releasing Se into aquatic systems are shale weathering processes and volcanoes.¹ The flux of Se from the ocean to the atmosphere represents, with volcanoes, the major source of atmospheric Se ($0.4\text{--}9 \times 10^3$ Se tons/year), with almost equal amounts released from the continents

Received: July 22, 2023

Revised: November 27, 2023

Accepted: November 27, 2023

Published: December 18, 2023



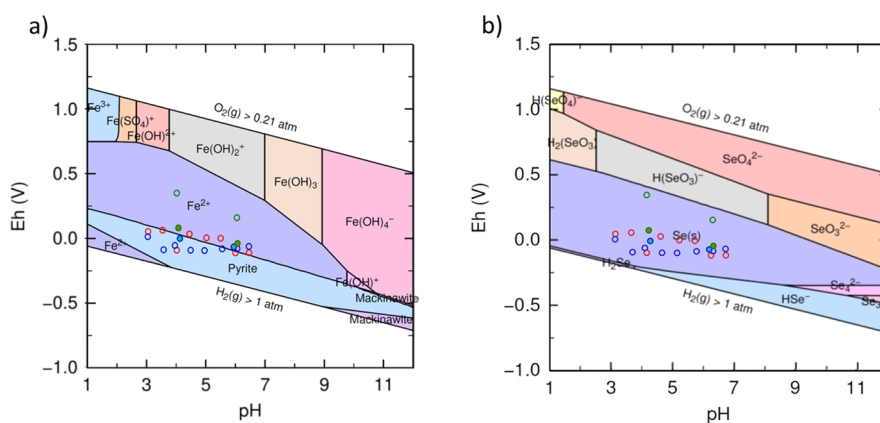


Figure 1. E_{H} -pH values collected in Se-pyrite experiments plotted in the (a) Fe-O-H and (b) Se-O-H E_{H} -pH diagrams. The E_{H} values for the experiments were plotted with empty red dots for pyrite titration data, empty blue dots for selenate experimental data, empty green dots for selenite experimental data, and blue and green filled dots for experimental sorption data of selenate and selenite in the presence of added sulfide. The predominance diagrams were generated with the public domain code PhreePlot,²⁰ using the version 10a of the thermodynamic database ThermoChimie (www.ThermoChimie-tdb.com). E_{H} -pH diagrams were constructed with 0.1 mM Se(VI), 1 mM Fe(II), 2 mM S(-II), and 10 mM NaCl.

($0.15\text{--}5.25 \times 10^3$ Se tons/year).¹¹ Several industries also contribute to the release of anthropogenic Se in natural waters: coal mining, glassmaking, irrigation, pigment production, petroleum refining, coal combustion, and disposal of radioactive waste.^{12–14} The last one is, in fact, a major source of the radioisotope ⁷⁹Se, a subproduct generated in nuclear power plants.

In aquatic systems, speciation of Se controls its reactivity, transport, bioavailability, and potential toxicity. The predominant species in oxic waters are the oxyanions: selenate [Se(VI)O_4^{2-}], selenite [Se(IV)O_3^{2-}], and biselenite [HSe(IV)O_3^-].¹⁵ Selenite is particularly bioavailable for most algae and cyanobacteria via phosphate transporters.¹⁶ Once internalized, it is converted to organic and volatile selenides.^{16,17} Two volatile Se species, dimethyl selenide (DMSe) and dimethyl diselenide (DMDSe), are the main forms present in the atmosphere.^{11,15} Selenium(VI) and Se(IV) can be sequestered by adsorption and reduction reactions down to Se(0, -I, and -II) by several minerals (clay, iron oxyhydroxides, iron sulfide) and natural organic matter.¹⁸ Selenium speciation in aquatic systems is governed by changes in pH and redox potential (E_{H}) (Figure 1). The chemical composition of the system, the type and amount of organic matter, and the microbiological activity also control the distribution of Se species in the environment.¹⁷ Thermodynamic calculations predict that selenate predominates in fully oxygenated water, while selenite and biselenite are predominant species of hypoxic water.¹⁹ Under reducing conditions, a large region of the E_{H} -pH diagram is occupied by reduced Se(0) species abiotically or biotically produced.¹⁷

Pyrite is the most abundant sulfide mineral and can be found in igneous, metamorphic, and marine sedimentary rocks as well as in submarine hydrothermal vents.²¹ The wide range of crystal chemical and surface properties displayed by pyrite—surface complexation, electron transfer, secondary mineral phases, short-range order, and structure sensitivity—makes this mineral an important redox catalyst for a multitude of reactions involving trace elements,²² such as uranium,²³ molybdenum,²⁴ arsenic,²⁵ Se,²⁶ and Tc.²⁷ A major environmental issue associated with the oxidation of pyrite is coal acid mine drainage. That process can release toxic trace elements in

aquatic systems.²⁵ In natural pyrite, different reduced Se species are present within or at the surface, like ferroselite (FeSe_2) and dzharkenite (FeSe).²⁸ Experimental studies demonstrated that Se(IV) can be reduced to Se(0) in contact with a pyrite surface under anoxic and acidic conditions.^{29,30} Probably, the electrons required for the reduction of Se(IV) are provided by the oxidation of Fe(II) and S(-II) phases.^{29,31,32} Few studies have investigated the reduction of Se(VI) by pyrite. Selenate adsorbs weakly on pyrite, making it challenging to characterize Se(VI)-pyrite interactions. The reduction of Se(VI) to Se(0) involves the transfer of six electrons and the breakdown of four oxygen bonds; consequently, the reductive sorption process is very slow, and pyrite might have a low reactivity with selenate ions.^{29,33} A complete and detailed understanding of the mechanisms involved in reducing Se(VI) and Se(IV) upon reaction with pyrite is still lacking.

To fill this knowledge gap, our goal was to thoroughly explore Se(VI) and Se(IV) interactions with pyrite to meticulously characterize all of the potential mechanisms involved, such as reductive adsorption and coprecipitation, over different times scales. Furthermore, the role of dissolved sulfide during the Se reduction and adsorption processes when reacted with pyrite was investigated.

MATERIALS AND METHODS

Chemicals. Sodium selenite, 99% (ref. 214485); sodium selenate, BioXtra (ref. S8295); zinc acetate dihydrate, $\geq 98\%$ (ref. 383058); carbon disulfide, anhydrous, 99+% (ref. 180173); sodium sulfide nonahydrate, $\geq 98\%$ (ref. 208043); sodium hydrosulfide hydrate (ref. 161527); iron(III) chloride hexahydrate, $\geq 99\%$ (ref. 31232); and sodium chloride, $\geq 99.5\%$ (ref. 71379), were obtained from Sigma-Aldrich. Sodium hydroxide, $\geq 98\%$ (ref. 6771.3), was purchased from Roth, and hydrochloric acid, 32% Extra Pure, SLR (ref. 10458790), and nitric acid, 67 to 70% trace metal grade (ref. A509P500), were from Fisher Chemical.

All solutions were prepared with boiled, nitrogen-degassed Millipore 18.2 M Ω /cm water and stored in an oxygen-free glovebox. All recipients were soaked in 5% HNO_3 for 24 h, cleaned for 10 min in an ultrasonic bath, and rinsed three times

with deionized water previously used. All experiments were done at room temperature in a Jacomex glovebox filled with Ar, with a controlled oxygen partial pressure below 5 ppm.

Pyrite and Se-Doped Pyrite Synthesis. Fresh pyrite was synthesized following the method proposed in previous literature.³⁴ Sixty milliliters of 0.05 M Fe(III) solution was added drop by drop into 60 mL of 0.15 M HS⁻ solution. Then, 1 M NaOH solution drops were added to maintain a pH value of ~4. The final solution was agitated for 5 days. The FeS₂ precipitate was decanted and washed by replacing the supernatant with a 0.2 M HCl solution six times, followed by acetone and carbon disulfide, to remove residual sulfur entirely from the solid surface. All of the washing solutions were in contact with pyrite for a 1 h minimum. Finally, the suspension was washed, vacuum filtered with a 0.22 μm filter with degassed water six times, dried in an anaerobic chamber, and kept in degassed ultrapure water at a 100 g/L solid concentration.

Se-doped pyrite synthesis was performed according to the method proposed by Diener and Neumann.³⁵ A precise amount of Se(VI) and Se(IV) stock solutions was added to the HS⁻ solution before being mixed with Fe(III) solution. Then, following the same steps, Se coprecipitated with pyrite was synthesized similarly to the protocol described above. The final concentrations used in synthesizing Se-pyrite samples were 50, 75, 100, 130, and 150 μM for Se(IV) and 50, 75, and 100 μM for Se(VI). The supernatant was acidified with 100 μL of 65% HNO₃ prior to elemental analysis.

Pyrite Titration and Se Sorption on Pyrite Experiments. Several batch experiments were conducted at different pH values (3–7.5), including a blank, which was prepared in glass bottles within an Ar anoxic atmosphere. The initial concentration of pyrite was fixed at 2 g/L, and the ionic strength was adjusted to 10 mM with NaCl. pH was adjusted to selected values by adding either HCl or NaOH and was measured by a pH meter with pH/°C probe with a 1 m cable (VWR pH110) calibrated with VWR buffers. After 24 h of equilibrium, the solution was decanted. Then, 2 × 10 mL was taken from all solutions and filtered with a 0.45 μm pore size membrane filter. The first volume was stored in a tube with 100 μL of a 100 mM zinc acetate dihydrate (ACZn) stock solution for Fe(II) and ΣS(-II). The second volume was acidified with 100 μL of 65% HNO₃ for inductively coupled plasma-atomic emission spectroscopy (ICP-AES) measurements. Similar experiments were carried out for Se(VI) sorption experiments, adding a concentration of 100 μM selenate and including a blank with the initial concentration of selenate.

Nine experiments were carried out following the same experimental protocol: six with Se(IV) and three with Se(VI). A sulfide solution of 1 mM was added from a stock solution of sulfide that was prepared by dissolving transparent crystals of Na₂S·9H₂O in degassed water. At the end of all batch experiments, pH and ORP values are measured (Figure 1). For all experiments, solid samples were collected after filtration, dried overnight, and preserved under an anoxic atmosphere.

Elemental Analysis. ICP-AES. Total Se and Fe concentrations in the supernatant samples were determined by ICP-AES (Varian 720 ES) at wavelengths of 234.350 and 238.204 nm for Fe and 196.026 nm for Se. 1000 ppm Fe and Se Roth standards were used to prepare an external calibration with a range of 0.01–25 ppm for Fe and Se concentrations, respectively. Analytical precision (RSD) and recovery (CMS)

were determined from replicate analyses ($n = 5$ and $n = 2$, respectively). The RSDs calculated for the 5 ppm standard were 1% for Fe and 1% for Se. The CMSs were 97% for Fe and 99% for Se. The detection limits (DLs) for Fe and Se were 0.1 and 0.7 μM, respectively. The quantification limits (QLs) for Fe and Se were 0.4 and 2.2 μM, respectively.

Colorimetric Methods. The ACZn solution samples were analyzed by colorimetric methods to measure the concentration of Fe(II) with the *o*-phenanthroline method³⁶ and ΣS(-II) with the sodium thiosulfate titration and methylene blue method.³⁷ Samples were analyzed at 513 and 670 nm for Fe(II) and ΣS(-II), respectively, with an Agilent Cary 300 UV-vis spectrophotometer. The DLs for Fe(II) and ΣS(-II) were 15.2 and 0.47 μM, respectively. The QLs for Fe(II) and ΣS(-II) were 46.1 and 1.47 μM, respectively.

Solid Characterization. XRD. X-ray powder diffraction (XRD) patterns were collected in the 20 to 70° 2θ range at room temperature using a laboratory Bruker D8 diffractometer with Cu radiation ($\lambda = 1.54 \text{ \AA}$), a SolX Si(Li) solid-state detector, and a step size of 0.026°. Into an airtight poly(methyl methacrylate) (PMMA) sample holder with a transparent dome to avoid any possible oxidation, samples were placed inside the glovebox. For all samples, the lattice parameters and the average crystallite sizes were calculated using the Debye-Scherrer equation and the Profex software,³⁸ with a free lattice parameter.

SEM. SEM images were collected with a scanning electron microscope with 16 kV at ISTerre, Grenoble, France. The sample was prepared by gently spreading a tiny quantity of pyrite on the surface of an electrically conductive carbon double-sided tape placed on the mount. The image detection mode used was backscattered electrons (BSEs) and secondary electrons (SEs).

BET. The specific surface area (SSA) was determined by the Brunauer-Emmett-Teller adsorption method (BET-N₂) at 77 K, using a Belsorp-Max (Bel Japan) volumetric gas sorption instrument. Inside the glovebox, 50 mg of pyrite was put in a glass cell and then dried under a vacuum at 80 °C for 12 h. The SSA was calculated from the BET equation in the P/P_0 range of 0.05–0.31.

XANES, EXAFS, and HERFD. X-ray absorption near-edge structures (XANES) and extended X-ray absorption fine structures (EXAFS) were collected at the Rossendorf Beamline operated by Helmholtz-Zentrum Dresden Rossendorf (HZDR, Germany).³⁹ High-energy-resolution fluorescence-detected (HERFD) X-ray absorption spectroscopy was performed at the French Absorption Spectroscopy Beamline in Material and Environmental Sciences at Ultra-High Dilution (FAME-UHD). For XANES and EXAFS samples, 100 mg of solid was homogenized with an agate mortar and then used to fill Kapton-sealed holders. For HERFD measurements, homogenized 40 mg of the solid samples and at least 10 mg of boron nitride were used to prepare 5 mm diameter pellets. All data collection was performed in a closed-cycle He cryostat with an atmosphere at 15 K to avoid photon-induced oxidation and to limit thermal disorder. XANES and EXAFS data were collected in fluorescence mode with an 18-element solid-state germanium detector (Ultra-LEGe, GUL0055, Mirion Technologies), and the Se references were in transmission mode recorded with an ionization chamber filled with a suitable gas mixture. HERFD, with a resolution of about 1–2 eV, used a beam with a size of 100 × 200 μm² and a 14-Si crystal analyzer spectrometer detection system. XANES and EXAFS spectra

were calibrated with the simultaneous measurement of Au foil at the L3 edge energy at 11,902.9 eV. For HERFD data calibration, a Se foil was used before and after each sample scan at a 12,658.1 eV energy reference. The data collected was processed with the open-source software ATHENA program.⁴⁰ Linear combination fit (LCF) was performed using the Se spectra of standards collected during the beamtime and previous beamtimes conducted in the same line. Data from the EXAFS region were analyzed using the Artemis software package. Theoretical models based on the structures of trigonal (gray) Se, ferroselite (FeSe₂), and S atom-centered pyrite were generated using the FEFF6 and ATOMS software packages to test for the existence of Se within or at the surface of pyrite.

THEORETICAL CALCULATIONS

All calculations were carried out with periodic boundary conditions (PBCs) in the plane-wave Vienna Ab initio Software Package (VASP)^{41,42} electronic structure code. The simulations were performed within the generalized gradient approximation (GGA) with the exchange-correlation functional of Perdew, Burke, and Ernzerhof (PBE).⁴³ The plane-wave calculations were carried out under the projector-augmented wave method with a kinetic energy cutoff of 400 eV.⁴⁴ The total energy convergence criteria were set to be within 1×10^{-5} eV with a Gaussian smearing width of 0.05 eV to improve the convergence of orbital energies. The vacuum region between the two (100) pyrite surfaces was set to 30 Å (unless stated otherwise) to remove spurious interactions between the adsorbate and the periodic image of the bottom layer of the surface (Figure 2).

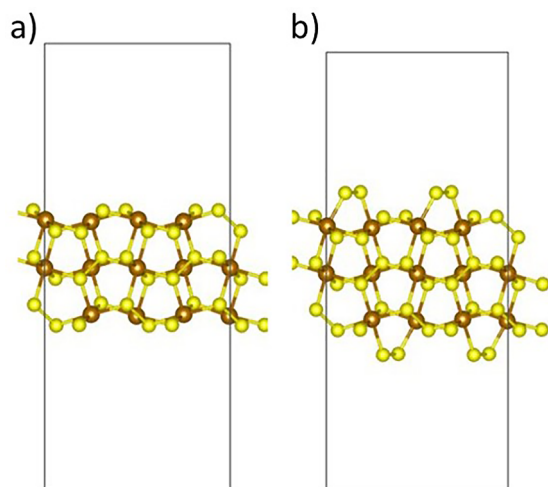


Figure 2. Side views of two different (100) pyrite surfaces: the neat surfaces (a) without disulfide terminations and (b) with disulfide terminations.

The adsorption energy of the adsorbate species, ΔE , was calculated using the following expression:

$$\Delta E = E_{\text{(pyrite slab)}} + E_{\text{adsorbate}} - E_{\text{total}} \quad (1)$$

where E_{total} represents the total energy of the pyrite slab with the molecule adsorbed on the surface, $E_{\text{(pyrite slab)}}$ the total energy of the slab, and $E_{\text{adsorbate}}$ the total energy of adsorbate in the gas phase (SeO₄²⁻, SeO₃²⁻, ...). Based on this definition, the larger the ΔE is, the more thermodynamically favorable the adsorption.

To investigate changes in the electronic structure when the molecule is adsorbed on the surface, the deformation charge density, $\Delta\rho(r)$, was calculated, which includes a direct comparison to the nonsorbed state:

$$\Delta\rho(r) = \rho_{\text{total}}(r) - (\rho_{\text{(pyrite slab)}}(r) + \rho_{\text{adsorbate}}(r)) \quad (2)$$

where $\rho_{\text{total}}(r)$, $\rho_{\text{(pyrite slab)}}(r)$, and $\rho_{\text{adsorbate}}(r)$ are electron densities of the total system, the silver slab, and the adsorbate in the gas phase, respectively.

The charge transfer was studied by comparing the Bader charges^{45–48} between the slab surface and the gas-phase molecule with the adsorbed state. The strength of bonds between the adsorbates and the surface was evaluated by calculating the charge density at (3,–1) bond critical points [$\nabla\rho(r)$]_{cp}, corresponding to the zero values of the gradient: $\nabla\rho(r) = 0$. These saddle points correspond to a minimum charge density along a bond path, providing a measure of the bonding strength, in terms of the electronic overlap.

RESULTS

Ab Initio Calculations. According to our calculations, the neat surface has the lowest adsorption energy (3.46 eV vs 1.44 eV) and therefore is a steadier adsorption surface. A bond appears to form between selenate and an iron atom of the pyrite surface in the adsorption process (Figure 3a). Thus, the remaining calculations were made on the selenate electronic properties adsorbed on the (100) neat surface.

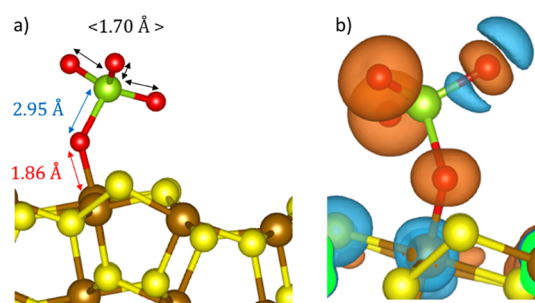


Figure 3. (a) Most stable adsorption configuration of selenate on the pyrite surface with the corresponding bond length. (b) Close-up of the charge deformation of the electron in the energy range between -2.5 and -0.5 eV at an isosurface value of $3.7 \times 10^{-2} \text{ e}^{-}\cdot\text{Å}^{-3}$.

Once adsorbed, the selenate ion undergoes a deformation induced by the 74% elongation of the Se–O bond involving the oxygen atom interacting with the pyrite surface, while the remaining part of the oxygen atoms does not experience a significant change in bond length (0.6% elongation). Interestingly, the Fe–O bond occurring at 1.86 Å is comparable to the original Se–O bond length found in selenate in the gas phase (Table S1), reflecting the strength of the Fe–O interaction. Neither the noninteracting O nor the Se shows a significant loss of Bader charges (<4%). Thus, the absence of significant differences in these Se–O bond lengths is not surprising.

Geometrically, the selenate molecule is slightly inclined regarding the pyrite surface with an angle of 130.31°, while the remaining oxygen atoms form an O–Se–O angle (113.88°), which is very similar to that of the SeO₃²⁻ molecule (113.78°). Moreover, the interacting O atom experiences a loss of charge

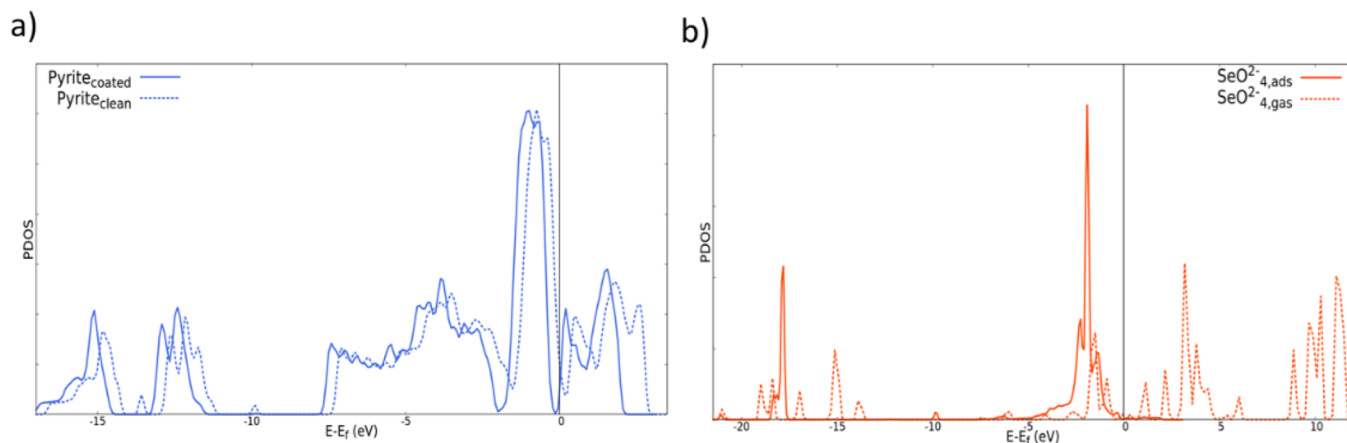


Figure 4. Projected density of states (PDOS) before (solid line) and after (dashed line) selenate adsorption for all orbitals of (a) the pyrite surface and (b) the selenate ion.

of $0.55 e^-$, 1 order of magnitude higher than those of the other O atoms, allowing the formation of a covalent Fe–O bond (Figure 3b). In Figure 3a, the blue area corresponds to a decrease in charge density, and the orange area is an increase in charge density at an isosurface value of $3.7 \times 10^{-2} e^- \cdot \text{\AA}^{-3}$, only observed in the oxygen atom furthest away from the pyrite surface. Interestingly, this O atom does not display a significant change in the Bader charge.

The projected density of states (PDOS) of both the pyrite surface and selenate ion shows that the adsorption phenomena shift the whole spectrum to lower energies (Figure 4). The pyrite's PDOS peaks at $-14.80, 12.15, -3.53, -0.75, 0.54,$ and 1.82 are shifted on average by -0.27 eV to the corresponding peaks at $-15.11, -12.40, -3.77, -0.98, 0.20,$ and 1.55 eV, respectively. Few gas-phase peaks disappear at $-13.58, -9.88,$ and 2.60 eV when selenate is adsorbed. The pyrite PDOS is mostly shifted in lower energies, whereas the selenate s orbital PDOS is completely changed. The selenate s orbital does not exhibit any density in unpopulated states and displays a density increase in the lowest energy states with three sharp peaks at $-21.12, -17.82,$ and -9.87 eV and a broader one at -5.22 eV. The p and d orbitals are the most revealing because they show a shift in the lower energies with minimal density unoccupied states. The shift amplitude is accompanied by a modification of the peak shape, which prevents an average estimation of the shift magnitude. However, both p and d orbitals experience in the energy range $[-2.5$ to $-0.5]$ eV, indicating for pyrite and selenate an increased state density following the adsorption.

Electrons for this energy range are the most susceptible to participating in chemical bonding; therefore, the spatial distribution of the electrons in this narrower energy range was examined. While the selenate ion forms a chemical bond with the pyrite surface, the bond between the O atom farthest from the surface and the rest of the molecule weakens as it loses electron density. This is consistent with the noticeable elongation of the Se–O of this involved O atom (1.71 \AA) compared to the two others not participating in the chemical bonding with pyrite (1.69 \AA) (Figure 3b).

Finally, the nudged elastic band method was used to calculate the energy cost of dissociating an O atom from the selenate ion interacting with pyrite (Figure 4), creating a series of snapshots along the dissociation path. The calculated energy barrier for this process was 4.56 eV in the dissociation direction.

However, the final image of the dissociation has a higher energy than the first image (difference of 1.55 eV).

Experimental Se Sorption on Pyrite. Pyrite Purity and Solubility. The XRD spectra (Figure 5, blue line) show mainly

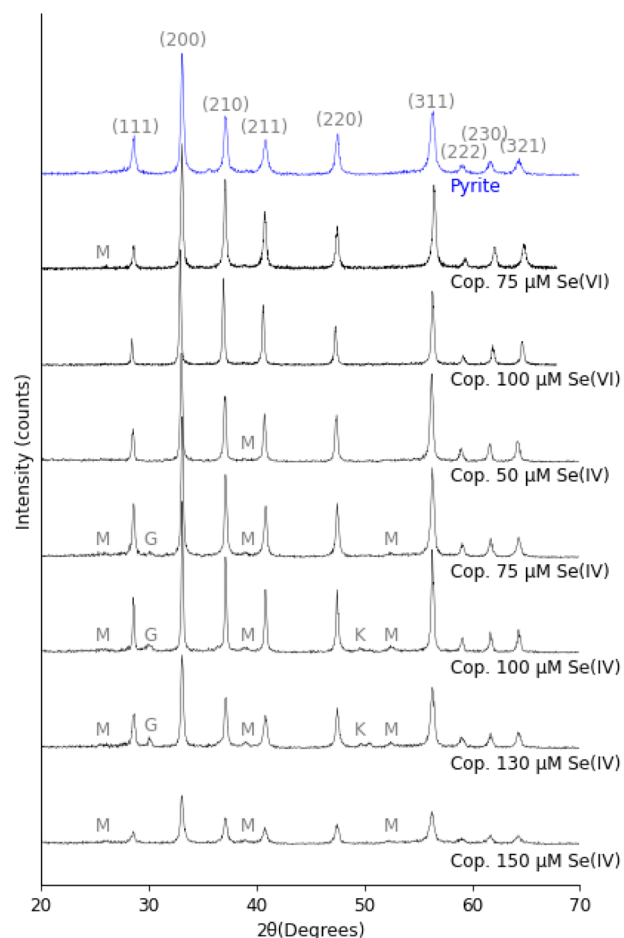


Figure 5. Raw data of XRD patterns measured from fresh pyrite and Se-doped pyrite syntheses (black line). The XRD peaks mainly show pyrite (blue line) and a minor fraction of marcasite (M), greigite (G), and mackinawite (K). The references used correspond to 00-016-0713 (I) for greigite, 00-042-1340 (*) for pyrite, PDF 86-0389 for mackinawite, and 00-037-0475 (*) for marcasite.

typical reflexes of the pure pyrite solid phase. Other peaks, displaying a lower magnitude, demonstrate the presence of other minerals (up to $\sim 20\%$), like marcasite, greigite, or mackinawite. The parameters obtained after the Rietveld refinements show a face-centered cubic unit cell parameter $a = 5.4245 \pm 1 \text{ \AA}$ (1) in good agreement with pyrite reference standards (00-037-0475 (*)). Crystallite sizes estimated from the Scherrer equation give values between $34.8 \pm 2.0 \text{ nm}$. The sharp diffraction peaks of the sample suggest good crystallinity. The SEM image (Figure S1) shows a large distribution of particles ranging from 500 nm to 2–3 μm . Finally, the SSA measured in the pyrite sample was $15 \text{ m}^2/\text{g}$.

SEM pictures show no changes in shape or size for pyrite equilibrated for 24 h at pH = 3, 5, or 7 (Figure S1). Fe(II) and $\sum\text{S}(-\text{II})$ concentrations for solutions equilibrated with pyrite at these different pH values are shown in Tables S2 and S3 and Figure 6. The measured Fe(II) concentrations ranged from 12

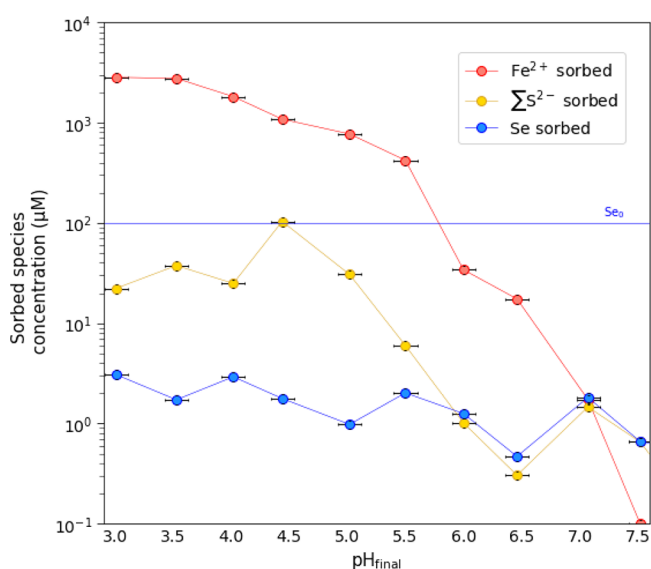


Figure 6. Sorbed measurement of Fe²⁺ (red dots), reduced sulfide species (yellow dots), and total selenium (blue dots), after 24 h equilibrium time with fresh pyrite at different pH between 3 and 7.5 in the presence of Se(VI), within sorption experiments. The error bar represents 0.1 pH measurement precision and 5% of the standard error for ICP–AES and UV–vis measurements.

to 2985 μM , close to the total Fe concentration value measured with ICP–AES (Table S2). The Fe(II) concentrations are higher at acidic pH. The $\sum\text{S}(-\text{II})$ values were below the DL for pH = 6.5 and 7.5 and equal to 105 μM at pH = 4.5. Sulfide levels were higher for acidic pH and tend to decrease below pH = 5. Measured E_{H} values ranged from -0.10 to 0.01 mV.

Se(VI) Adsorption on Pyrite. In Se adsorption experiments, Fe(II) concentrations (Tables S2 and S3) were similar to total Fe concentrations for different pH values. The disparity between Fe(II) and total Fe measurements corresponds to a 5% standard error in both UV–vis and ICP–AES measurements. In the Se-free experiments, the Fe(II) concentrations were 20 times higher at high pH and up to 50 times higher at low pH (Table S2). As expected, the concentrations of Fe(II) are higher for lower pH values (3–6) than for neutral pH values (6.5–7.5). Sulfide concentrations ranged from ~ 0.5 to $\sim 15 \mu\text{M}$ and were higher at acidic pH. They displayed lower concentrations for experiments where Se was present,

indicating sorbed concentration in the pyrite solid (Figure 6). The concentrations of adsorbed Se(VI) on pyrite varied between 1 (pH = 5) and 6.4 μM (pH = 3). Despite the low adsorption of Se(VI) within 24 h ($<2\%$), a slightly improved adsorption capacity is observed for acidic conditions (2–6% Se sorbed, pH < 4.5). Finally, the measured E_{H} values were between -0.09 and 0.01 V (Figure 1).

No significant difference was observed for XANES-determined Se speciation for the samples equilibrated at pH 4 and 6. The white lines (E_{max}) for the XANES spectra for both samples are located between the E_{max} values for the Se(IV) and Se(0) standards (Figure S2a, Table S5). The LCF results show that these two samples are composed of trigonal, gray Se(0) ($\sim 80\%$) and Se(IV) ($\sim 20\%$) (Table S4). Similar results were found using HERFD–XANES for Se(VI) adsorbed on pyrite at pH 4 (see Figure S2b and Table S5).

Sulfide Influence on Se Adsorption. In the presence of sulfide, Se(VI) adsorption on pyrite remains unchanged, and no enhancement is found. E_{H} values were 0.00 and -0.07 V for pH = 4 and 6, respectively. The XANES and HERFD–XANES findings additionally indicate that the samples primarily consist of trigonal gray Se(0) with a minor presence of Se(IV) (Figure S2). In contrast with Se(VI), large Se(IV) adsorption on pyrite is observed ($\sim 40\%$ improvement at pH = 6 and $\sim 60\%$ improvement at pH = 4). The removal of Se(IV) when interacting with pyrite from both solutions (pH 4 and 6) was beyond 95% (Figure S3). The speciation of Se was a mix of Se(IV) and Se(0) (Table S3 and Figure S2). The measured E_{H} values for the experiments without sulfide and experiments with sulfide ranged from 0.35 to 0.16 V and from 0.08 to -0.04 V, respectively.

Selenium Coprecipitation with Pyrite. Similarly, to pure pyrite, the XRD diffractions show mainly peaks ($\sim 80\%$) associated with pure pyrite yet with some impurities of marcasite, greigite, and mackinawite mineral phases (Figure 5). No significant difference between the mesh parameters or the particle size was found concerning the pyrite sample reference. Sharper peaks were observed for samples coprecipitated with 50, 75, and 100 μM Se(IV) and with 75 and 100 μM Se(VI). The samples with 130 and 150 μM Se(IV) and 50 μM Se(VI) showed less pronounced peaks, indicating a lower crystallinity than that of pure pyrite.

All of these samples display similar XANES features, suggesting that the Se speciation results from a mix of Se(IV) and Se(0) (Table S3). HERFD–XANES spectra revealed distinct spectral features not observed in normal XANES spectroscopy. Notably, three additional features are evident in the coprecipitation samples: a form similar to the reference FeSe₂, a white line and shape of the 100 μM Se(IV) coprecipitated sample resembling the reduced Se peak of the Se(IV) adsorption sample equilibrated at pH 6 with sulfur addition, and analogous shape and energy characteristics between samples of Se(IV) adsorption equilibrated at pH 6 without sulfur addition and the 76 μM Se coprecipitated sample (Figures S2 and S4 and Table S5).

For 50, 75, and 100 μM Se(IV) samples (about 1325, 1974, and 4037 ppm) measured with EXAFS (Figure 7), the crystal structures used for the fit are chosen considering (1) the sample matrix and (2) the possible choices of Se species that can be formed. The references used consisted of the pyrite structure⁴⁹ involving a substitution of the central S atom by a Se atom,^{26,50} trigonal selenium (Se(0)), and ferroselite (Se(-I)). The most appropriate fit of the spectra used the

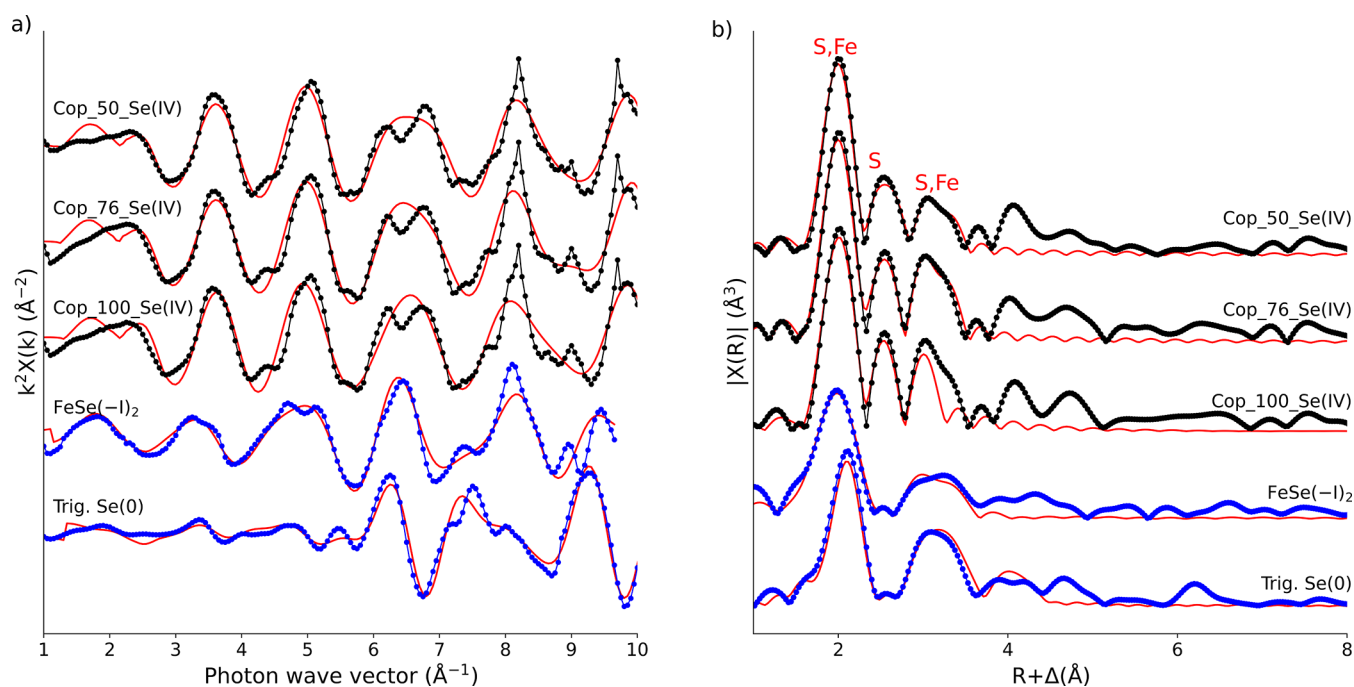


Figure 7. (a) k^2 -weighted chi functions of EXAFS spectra and (b) the Fourier transform magnitudes of Se K-EXAFS spectra measured at the Se K edge of Se(IV)-doped pyrite. The fit is represented by red lines.

Table 1. EXAFS Parameters and Interatomic Distances Calculated for Se(IV)–Pyrite Coprecipitation Samples

sample	path	N^a	R^b (Å)	σ^2^c (Å ²)	ΔE_0^d (eV)	$S_0^2^e$	R factor
Cop_50 μM r range: 1.45–3.5	Se–S.1	1.0	2.26 (0.04)	0.003 ^a	6.58 (1.22)	0.898 (0.070)	0.014
	Se–Fe.1	3.0	2.31 (0.01)	0.003 ^a	6.58 (1.22)	0.898 (0.070)	
	Se–S.2	6.0	3.12 (0.02)	0.006 (0.002)	6.58 (1.22)	0.898 (0.070)	
	Se–S.3	6.0	3.36 (0.03)	0.006 (0.004)	6.58 (1.22)	0.898 (0.070)	
	Se–Fe.2	3.0	3.50 (0.03)	0.005 (0.003)	6.58 (1.22)	0.898 (0.070)	
Cop_76 μM r range: 1.3–3	Se–S.1	1.0	2.25 (0.03)	0.003 ^a	6.09 (0.77)	0.954 (0.064)	0.017
	Se–Fe.1	3.0	2.31 (0.01)	0.003 ^a	6.09 (0.77)	0.954 (0.064)	
	Se–S.2	6.0	3.10 (0.01)	0.005 (0.001)	6.09 (0.77)	0.954 (0.064)	
	Se–S.3	6.0	3.35 (0.01)	0.003 ^a	6.09 (0.77)	0.954 (0.064)	
	Se–Fe.2	3.0	3.48 (0.01)	0.003 ^a	6.09 (0.77)	0.954 (0.064)	
Cop_100 μM r range: 1.1–3.3	Se–S.1	1.0	2.26 (0.04)	0.003 ^a	6.51 (1.45)	0.900 (0.090)	0.024
	Se–Fe.1	3.0	2.32 (0.01)	0.003 ^a	6.51 (1.45)	0.900 (0.090)	
	Se–S.2	6.0	3.10 (0.02)	0.004 (0.003)	6.51 (1.45)	0.900 (0.090)	
	Se–S.3	6.0	3.33 (0.06)	0.003 ^a	6.51 (1.45)	0.900 (0.090)	
	Se–Fe.2	3.0	3.41 (0.66)	0.023 (0.042)	6.51 (1.45)	0.900 (0.090)	

^aCoordination number for single paths, fixed value. ^bInteratomic distance. ^cDebye–Waller factor. ^dShift of energy threshold. ^ePassive electron reduction factor.

five first single scattering paths of pyrite: Se–S.1 = 2.28 Å, Se–Fe.1 = 2.31–2.32 Å, Se–S.2 = 3.10–3.11 Å, Se–S.3 = 3.34, and Se–Fe.2 = 3.47–3.49 Å (Table 1). The atomic distances between the paths are similar to the values found by Manceau et al. (2020) in a natural pyrite with 500 ppm of Se, and a little shorter than the values of Matamoros-Veloza et al. (2014), also in a natural euhedral pyrite with 670 ppm of Se.

DISCUSSION

Se(VI)–Pyrite Interactions. *Initial Adsorption from Ab Initio Calculations.* Two reactive cleavage surfaces can be studied in *ab initio* calculations. The cleavages consist of one surface with disulfide atoms and one corresponding to a neat surface without disulfide. These two possible surfaces in the [100] plane cannot be compared due to the difference in the

electron number between the two systems. The surface with disulfide terminations is discarded for several reasons, such as the low energy found when the Fe–S sulfurs start to join and disulfide bonds are formed, which explains why there is no experimental evidence of a pyrite surface with a nonnegligible amount of single Fe–S terminations. Furthermore, when the surface is more suitable for adsorption, the disulfide surface presents the highest adsorption energy, which makes it less stable (3.46 vs 1.44 eV). The last argument discussed further down is related to the adsorption of selenate, where a bond with a Fe atom is most likely to be involved (Figure 3a).

Regarding the interaction of Se(VI) with pyrite, it is theoretically feasible in terms of energy that the neat pyrite surface adsorbs the selenate molecule with an energy of 3.46 eV, promoting the creation of a bond between a Fe atom from

the pyrite surface and an O atom from selenate. Selenate deforms due to the elongation caused by the strong interaction that Fe has with O, which corresponds to a covalent bond, with an energy loss of $0.55 e^-$ observed in the respective oxygen. The new selenate geometry corresponds to the angles detected in the reduced selenite molecule, which may indicate that once adsorption is done within the first nanoseconds, reduction to selenite and oxidation of the pyrite surface are likely to follow.

PDOS analysis shows that the atomic distance of the O atom further away from the pyrite increases in charge density, but because there is no significant change in the Bader charge, it must be compensated for either by the deeper orbitals or by weakening its Se–O bond. The Se–O bond of this distant atom appears to weaken and, consequently, to elongate to a distance of 1.71 Å, compared to 1.69 Å for the other two O atoms that do not interact with pyrite. However, it should be noted that a single O atom in the gas phase is highly unstable. Provided that the furthest O atom from the pyrite surface is removed from the water molecule, a strong reaction with the surrounding solvent will occur. In addition, PDOS results indicate significant changes, especially in the p and d orbitals of both pyrite and selenate: lower energies with very few unoccupied density states and an increase of the density of states in the energy range between -2.5 and -0.5 eV, the energy range most likely to participate in a chemical bond. Further analysis of the projected state density between a hydrated selenate molecule and a neat pyrite surface is strongly recommended for a better understanding.

Factors Controlling Se(VI) Reductive Adsorption Processes over 24 h. As indicated above, the first reaction between selenate and pyrite occurs within nanoseconds. However, the minimum equilibrium time that can be experimentally considered is 24 h, in line with the analytical methods used. After this 24 h period, the final solid had a selenium concentration just above the DL.

The interaction of Se(VI) with pyrite is significantly influenced by the synthesized pyrite product. Pyrite formation at low temperatures consists of the dilution–precipitation pathway of intermediate phases such as nanomackinawite and nanogreigite.⁵¹ This occurs via a reductive coprecipitation pathway where Fe(III) is reduced to Fe(II) by S(–II), which is first oxidized to S(0) polysulfides and then to S(–I). The high solubility of pyrite measured at acidic pH during the pyrite titration experiments suggests that the precipitate corresponds to a “fresh pyrite” or a “poorly” crystallized pyrite and it may contain metastable nanominerals from precursor phases. Similarly, previous research reported elevated Fe concentrations after dissolving synthesized pyrite ($pH < 5$).⁵² These findings align with a prior study,⁵³ demonstrating that the stability of iron sulfides and their dissolution in ferruginous waters vary as a function of crystal size, pH, E_H , and aging time.⁵³ These nanosized mineral phases can also explain the higher SSA found ($15 m^2/g^{-1}$) than those previously documented in natural pyrites ($m^2/g^{-154-57}$) with a better crystallization. High concentrations of Fe(II) were not determined for alkaline conditions because iron sulfides are more soluble under acidic conditions and Fe(II) is soluble below pH 7.

Due to its inert character and negative charge, it is not surprising that only less than 10% of Se(VI) was adsorbed and that the highest observed removal occurred at $pH < 6$. Se adsorption appears to have decreased the dissolved concentrations of Fe(II) and $\sum S(-II)$ compared to those measured

in the absence of selenium, as seen in Figure 6 and Tables S2 and S3. Selenium(VI) reduction or complexation in solution is discarded because there is no evidence of direct selenate sequestration with aqueous S(–II) in previous studies to the best of our knowledge, and after performing some blanks with 250 mM $\sum S(-II)$ and 250 μM SeO_4^{2-} , at $pH = 6$ and 7, no Se(VI) precipitation was observed over six months. It is possible that Se(VI) and Fe(II) could precipitate, complex or form ternary surface complexes. After comparing the ion product to the only constant found in literature for $FeSeO_{4(s)}$ ^{58,59} ($K = 0.0015$), the Se(VI)–pyrite system is not sufficiently saturated to form the precipitate. The influence of adding sulfide regarding Se(VI) adsorption is negligible in terms of the percentage of Se(VI) adsorbed or speciation. Similar findings were found in a previous study but adding Fe(II) to Se(VI) sorption experiments on pyrite, where the presence of Fe(II) did not improve Se(VI) removal.³⁰ XANES spectroscopy results show a reduction of Se(VI) adsorbed adding or not sulfide on pyrite, mainly as Se(0), close to those from other studies.^{30,60} This finding is further supported by the measured E_H values plotted in the Pourbaix diagrams located within the domains of stability of Se(0) and pyrite (Figure 1).

In the reductive adsorption processes of Se(VI), a slightly more soluble polymorph of pyrite should not be neglected, even when it constitutes less than 20% of the composition. Previous studies on the reduction of Tc in marcasite–pyrite and natural pure pyrite have given different results, in which the presence of marcasite slowed down the reduction.⁶¹ Consequently, it is strongly recommended that additional research be conducted to explore the reactivity of Se(VI) in conjunction with Fe(II) and marcasite.

Our coprecipitation experiment with Se(VI) was not successful. The removal was minimal, and the quality of the collected XANES data was poor. It seems that the small amount of Se(VI) that reacted was reduced to Se(0).

Factors Controlling Se(IV) Interaction with Pyrite. Se(IV) Adsorption Experiments. Sulfide enhances the removal of Se(IV). This enhancement is not surprising since prior work shows that after 30 min, 5 mM sulfide reduces and precipitates 97.3% (± 3.7) from 0.11 mM Se(IV) to Se(0).³² On the other hand, Fe(II) released by pyrite can also influence the amount of Se(IV) removed. The concentration of dissolved Fe(II) (measured) saturated the batch solution according to the $FeSeO_3$ solubility constant ($K = 10^{-9.99}$) and could have led to the precipitate formation (as observed on clay; see refs 59 and 62). Supporting the potential formation of $FeSeO_3$, our new HERFD–XANES results do indicate the presence of Se(IV) and Se(0) only for the Se(IV) experimental products, independent of the presence of sulfide. Moreover, in the samples without sulfide, at $pH = 4$, which display a higher concentration of dissolved Fe(II), the percentage of removed Se(IV) is higher. In agreement, the E_H values plotted on the Pourbaix diagrams indicate an equilibrium phase close to the boundaries between Se(0), $H(SeO_3)^-$, and Fe(II).

Se(IV)-Doped Pyrite. The coprecipitation of Se(IV) with pyrite is a fast and efficient process, as demonstrated by prior studies.^{35,63} Se(IV) coprecipitation at the three concentrations studied, as revealed by XANES and EXAFS results, exhibits indistinguishable local structural parameters. This suggests a consistency in both chemical composition and crystal structure even when examining samples doped with up to 4037 ppm of Se. The XANES peak for all three samples investigated in our study is located between Se(IV) and Se(0) and with a similar

shape to the trigonal Se reference. On the other hand, HERFD–XANES mainly indicates the presence of a Se(–I) due to the similarity of the shape to the FeSe(–I)₂ reference. The correspondence between the white line HERFD–XANES spectra of pyrite doped with 100 μM Se(IV) with the spectrum of the Se(IV) sample adsorbed at pH 6 adding sulfur suggests a possible formation of SeS₂ on the pyrite surface due to an excess of Se. This observation can also be supported by the fact that the EXAFS fit obtained with 100 μM Se(IV) was less optimal, accompanied by a slightly elevated Debye–Waller factor and *R* factor. Comparable findings were reported for samples prepared with a similar protocol.⁶³ Nevertheless, it is unclear whether Se is reduced to Se(–I) or Se(0).⁶³ On the other hand, our EXAFS results suggest that Se replaces a S in the pyrite structure, analogous to the previous natural Se–pyrite studied by Manceau et al. (2020) and Matamoros-Veloza et al. (2014) where Se is reduced to Se(–I) based on stoichiometry. This is different from the Diener et al. study that concluded the incorporation of Se as amorphous Se(0) with a Se neighbor in the coordination layer at ~2.3 Å.⁶³ It remains uncertain if this disparity is due to a different EXAFS adjustment strategy or different experimental conditions.

The main host for Se is iron minerals, predominantly pyrite, found in shales. Selenate and selenite become toxic at elevated concentrations, often originating from anthropogenic sources such as coal mining or radioactive waste. Our new findings suggest that the addition of S(–II) enhances the adsorption of pyrite, proving to be an effective treatment for removing Se(IV) from polluted water or mining waste. However, the pyrite reductive adsorption mechanism demonstrates significantly greater efficiency for Se(IV) compared to Se(VI). To address the reversible desorption of Se, the reduction of both Se(VI) and Se(IV) to low-solubility Se(0) or other reduced Se species (Se(–I), Se(–II)) offers a stable solution, surpassing the efficacy of mere complexation or adsorption of the original oxyanions. Furthermore, integrating selenium within the pyrite stoichiometric structure may emerge as a more effective treatment avenue. This approach has the potential to minimize the mobility of precipitated, reduced Selenium species, as demonstrated by Poulain et al. in 2022.⁶⁴ Considering the low reactivity of Se(VI) with pyrite, a promising strategy for future studies to enhance removal involves incorporating zero-valent iron. Zero-valent iron appears to facilitate the conversion of Se(VI) into Se(IV) and Se(0), thereby enhancing selenium reduction processes.⁶⁵

Se has emerged as a promising paleo-redox proxy in marine sediments due to its heightened concentration in anoxic environments, elevated redox potential, and sensitivity to both global and regional perturbations over relatively short time scales.^{5,66} This study marks a significant advance in our understanding of ancient processes leading to selenium accumulation in pyrite within sulfidic environments. It reveals a pathway involving oxyanion reduction to Se(0) and Se(–I), shedding light on intricate mechanisms. The detailed mechanism explored in this study includes reductive adsorption, Se incorporation in the pyrite lattice, and sulfide precipitation, laying valuable groundwork for future Se isotopic studies in both natural and experimental samples. This forthcoming research, complementing our investigation, holds the potential to deepen our understanding of the mechanisms elucidated here and capture the occurrences of anoxic events, spanning from modern times to earth's stepwise oxygenation.

■ ASSOCIATED CONTENT

SI Supporting Information

The Supporting Information is available free of charge at <https://pubs.acs.org/doi/10.1021/acsearthspacechem.3c00219>.

Bond parameters of atoms in the gas and hydrated phases for the selenate ion; SEM images of the pyrite solid before and after Se(VI) sorption experiments; aqueous concentrations of selenium, iron, and sulfur in Se–pyrite experiments; XANES and HERFD–XANES selenium K-edge spectra and linear combination fitting of selenium K-edge XANES spectra (PDF)

■ AUTHOR INFORMATION

Corresponding Authors

Anthony Chappaz – STARLAB, Central Michigan University, Mount Pleasant, Michigan 48859, United States; orcid.org/0000-0001-8713-8456; Email: anthony.c@cmich.edu

Laurent Charlet – ISTERre, Univ. Grenoble Alpes, Univ. Savoie Mont Blanc, CNRS, IRD, Univ. Gustave Eiffel, Grenoble 38058, France; orcid.org/0000-0003-3669-7316; Email: charlet38@gmail.com

Authors

Carolina Guida – ISTERre, Univ. Grenoble Alpes, Univ. Savoie Mont Blanc, CNRS, IRD, Univ. Gustave Eiffel, Grenoble 38058, France; STARLAB, Central Michigan University, Mount Pleasant, Michigan 48859, United States; Grupo geología médica y forense, Universidad Nacional de Colombia, Bogotá 111321, Colombia; orcid.org/0000-0002-3181-7860

Vivien Ramothe – ISTERre, Univ. Grenoble Alpes, Univ. Savoie Mont Blanc, CNRS, IRD, Univ. Gustave Eiffel, Grenoble 38058, France; orcid.org/0000-0003-4614-2226

Pauline Simonnin – Physical Sciences Division, Physical and Computational Sciences Directorate, Pacific Northwest National Laboratory, Richland, Washington 99352, United States; orcid.org/0000-0002-6197-7435

Kevin M. Rosso – Physical Sciences Division, Physical and Computational Sciences Directorate, Pacific Northwest National Laboratory, Richland, Washington 99352, United States; orcid.org/0000-0002-8474-7720

Rong-Rong Ding – ISTERre, Univ. Grenoble Alpes, Univ. Savoie Mont Blanc, CNRS, IRD, Univ. Gustave Eiffel, Grenoble 38058, France; CAS Key Laboratory of Urban Pollutant Conversion, Department of Environmental Science and Engineering, University of Science and Technology of China, Hefei 230026, China

Damien Prieur – The Rossendorf Beamline at ESRF, Grenoble 38043, France; HZDR Institute of Resource Ecology, Dresden 01328, Germany; orcid.org/0000-0001-5087-0133

Andreas C. Scheinost – The Rossendorf Beamline at ESRF, Grenoble 38043, France; HZDR Institute of Resource Ecology, Dresden 01328, Germany; orcid.org/0000-0002-6608-5428

Complete contact information is available at: <https://pubs.acs.org/doi/10.1021/acsearthspacechem.3c00219>

Author Contributions

C.G. and V.R. are cofirst authors. The manuscript was written through the contributions of all authors. All authors have approved the final version of the manuscript.

Funding

The project funding and laboratory equipment have been supported by a grant from the French National Radioactive Waste Management Agency (ANDRA, Chatenay-Malabry). C.G. has received support funding from Convocatoria 885, Ministry of Science, Technology, and Innovation, Colombia. V.R. was supported by a SERENADE project award for the postdoctoral fellowship. The work was also funded by NSF-EAR Grant 2051199 awarded to A.C.

Notes

The authors declare no competing financial interest.

ACKNOWLEDGMENTS

The authors are thankful to the geochemistry–mineralogy platform of ISTerre (Grenoble, France) for laboratory support. The authors thank Valérie Magnin and Nathaniel Findling for performing BET and XRD measurements. K.M.R. and P.S. acknowledge the support from the US Department of Energy (DOE) Office of Science, Office of Basic Energy Sciences, Chemical Sciences, Geosciences, and Biosciences Division through its Geosciences programs at the Pacific Northwest National Laboratory (PNNL). V.R. thanks Dr. Ben Gilbert for support with *ab initio* calculations. The PNNL is a multiprogram national laboratory operated for DOE by the Battelle Memorial Institute under Contract DE-AC05-76RL0-1830. We acknowledge the European Synchrotron Radiation Facility (ESRF) for the provision of synchrotron radiation facilities, and we would like to thank beamline BM20 and BM16 for assistance and support. We thank Mauro Rovezzi for their invaluable help during our measurements at BM30. We would like to thank the anonymous reviewers for their valuable comments, which helped to improve the quality of this article.

ABBREVIATIONS

BET, Brunauer–Emmett–Teller adsorption method; ICP–AES, inductively coupled plasma–atomic emission spectroscopy; XRD, X-ray diffraction; RSD, relative standard deviation; DLs, detection limits; QLs, quantification limits; BSEs, backscattered electrons; SEs, secondary electrons; SSA, specific surface area; PMMA, poly(methyl methacrylate); XAS, X-ray absorption spectroscopy; XANES, X-ray absorption near-edge structure; EXAFS, extended X-ray absorption fine structure; HERFD, high-energy-resolution fluorescence-detected X-ray absorption spectroscopy; LCF, linear combination fit; PBC, periodic boundary conditions; VASP, Vienna Ab initio Software Package; GGA, generalized gradient approximation; PBE, Perdew, Burke, and Ernzerhof; ΔE , adsorption energy of the adsorbate species; $\Delta\rho(r)$, deformation charge density; PDOS, projected density of states

REFERENCES

(1) Fernández-Martínez, A.; Charlet, L. Selenium Environmental Cycling and Bioavailability: A Structural Chemist Point of View. *Rev. Environ. Sci. Biotechnol.* **2009**, *8* (1), 81–110.
(2) Fordyce, F. M. Selenium Deficiency and Toxicity in the Environment. In *Essentials of Medical Geology: Revised Edition*; Selinus, O., Ed.; Springer Netherlands: Dordrecht, 2013; pp 375–416. DOI: 10.1007/978-94-007-4375-5_16.

(3) Chen, F.; Burns, C. P.; Ewing, R. C. 79Se: Geochemical and Crystallo-Chemical Retardation Mechanisms. *J. Nucl. Mater.* **1999**, *275* (1), 81–94.
(4) Scheinost, A. C.; Charlet, L. selenite Reduction by mackinawite, Magnetite and Siderite: XAS Characterization of nanosized Redox Products. *Environ. Sci. Technol.* **2008**, *42* (6), 1984–1989.
(5) Stüeken, E. E.; Kipp, M. A. Selenium Isotope Paleobiogeochemistry; Elements in Geochemical Tracers in Earth System Science. Cambridge University Press 2020. DOI: 10.1017/9781108782203.
(6) El-Ramady, H.; Abdalla, N.; Taha, H. S.; Alshaal, T.; El-Henawy, A.; Faizy, S. E.-D. A.; Shams, M. S.; Youssef, S. M.; Shalaby, T.; Bayoumi, Y.; Elhawat, N.; Shehata, S.; Sztrik, A.; Prokisch, J.; Fari, M.; Domokos-Szabolcsy, E.; Pilon-Smits, E. A.; Selmar, D.; Haneklaus, S.; Schnug, E. Selenium and Nano-Selenium in Plant Nutrition. *Environ. Chem. Lett.* **2016**, *14* (1), 123–147.
(7) WHO. Trace elements in human and health. https://scholar.google.com/scholar_lookup?title=Trace%20elements%20in%20human%20nutrition%20and%20health&publication_year=1996 (accessed 2021–10–12).
(8) Reich, H. J.; Hondal, R. J. Why Nature Chose Selenium. *ACS Chem. Biol.* **2016**, *11* (4), 821–841.
(9) Chapman, L. M.; Roling, J. A.; Bingham, L. K.; Herald, M. R.; Baldwin, W. S. Construction of a Subtractive Library from Hexavalent Chromium Treated Winter Flounder (*Pseudopleuronectes Americanus*) Reveals Alterations in Non-Selenium Glutathione Peroxidases. *Aquatic Toxicology* **2004**, *67* (2), 181–194.
(10) Balistrieri, L. S.; Chao, T. T. Adsorption of Selenium by Amorphous Iron Oxyhydroxide and Manganese Dioxide. *Geochim. Cosmochim. Acta* **1990**, *54* (3), 739–751.
(11) Wen, H.; Carignan, J. Reviews on Atmospheric Selenium: Emissions, Speciation and Fate. *Atmos. Environ.* **2007**, *41* (34), 7151–7165.
(12) Cao, S.; Duan, X.; Zhao, X.; Ma, J.; Dong, T.; Huang, N.; Sun, C.; He, B.; Wei, F. Health Risks from the Exposure of Children to As, Se, Pb and Other Heavy Metals near the Largest Coking Plant in China. *Science of The Total Environment* **2014**, *472*, 1001–1009.
(13) Etteieb, S.; Magdoui, S.; Komtchou, S. P.; Zolfaghari, M.; Tanabene, R.; Brar, K. K.; Calugaru, I. L.; Brar, S. K. Selenium Speciation and Bioavailability from Mine Discharge to the Environment: A Field Study in Northern Quebec, Canada. *Environ. Sci. Pollut. Res.* **2021**, *28* (36), 50799–50812.
(14) Grambow, B. Mobile Fission and Activation Products in Nuclear Waste Disposal. *Journal of Contaminant Hydrology* **2008**, *102* (3–4), 180–186.
(15) Mason, R. P.; Soerensen, A. L.; DiMento, B. P.; Balcom, P. H. The Global Marine Selenium Cycle: Insights From Measurements and Modeling. *Global Biogeochemical Cycles* **2018**, *32* (12), 1720–1737.
(16) Vriens, B.; Behra, R.; Voegelin, A.; Zupanec, A.; Winkel, L. H. E. Selenium Uptake and Methylation by the Microalga *Chlamydomonas Reinhardtii*. *Environ. Sci. Technol.* **2016**, *50* (2), 711–720.
(17) Simmons, D. B. D.; Wallschläger, D. A Critical Review of the Biogeochemistry and Ecotoxicology of Selenium in Lotic and Lentic Environments. *Environ. Toxicol. Chem.* **2005**, *24* (6), 1331–1343.
(18) Perrone, D.; Monteiro, M.; Nunes, J. The Chemistry of Selenium; 2015; pp 3–15. DOI: 10.1039/9781782622215-00003.
(19) Belzile, N.; Chen, Yu.-W.; Xu, R. Early Diagenetic Behaviour of Selenium in Freshwater Sediments. *Appl. Geochem.* **2000**, *15* (10), 1439–1454.
(20) Kinniburgh, D. G.; Cooper, D. M. *Creating Graphical Output with PHREEQC*; NERC Open Research Archive 2009.
(21) Berner, R. A. Sedimentary Pyrite Formation: An Update. *Geochim. Cosmochim. Acta* **1984**, *48* (4), 605–615.
(22) Rickard, D.; Luther, G. W. Chemistry of Iron Sulfides. *Chem. Rev.* **2007**, *107* (2), 514–562.
(23) Descostes, M.; Schlegel, M. L.; Eglizaud, N.; Descamps, F.; Miserque, F.; Simoni, E. Uptake of Uranium and Trace Elements in Pyrite (FeS₂) Suspensions. *Geochim. Cosmochim. Acta* **2010**, *74* (5), 1551–1562.

- (24) Chappaz, A.; Lyons, T. W.; Gregory, D. D.; Reinhard, C. T.; Gill, B. C.; Li, C.; Large, R. R. Does Pyrite Act as an Important Host for Molybdenum in Modern and Ancient Euxinic Sediments? *Geochim. Cosmochim. Acta* **2014**, *126*, 112–122.
- (25) Nyström, E.; Thomas, H.; Wanhainen, C.; Alakangas, L. Occurrence and Release of Trace Elements in Pyrite-Rich Waste Rock. *Minerals* **2021**, *11* (5), 495.
- (26) Manceau, A.; Merkulova, M.; Mathon, O.; Glatzel, P.; Murdzek, M.; Batanova, V.; Simionovici, A.; Steinmann, S. N.; Paktunc, D. The Mode of Incorporation of As (-I) and Se (-I) in Natural Pyrite Revisited. *ACS Earth and Space Chemistry* **2020**, *4* (3), 379–390.
- (27) Rodríguez, D. M.; Mayordomo, N.; Scheinost, A. C.; Schild, D.; Brendler, V.; Müller, K.; Stumpf, T. New Insights into ⁹⁹Tc(VII) Removal by Pyrite: A Spectroscopic Approach. *Environ. Sci. Technol.* **2020**, *54* (5), 2678–2687.
- (28) Ryser, A. L.; Strawn, D. G.; Marcus, M. A.; Johnson-Maynard, J. L.; Gunter, M. E.; Müller, G. Micro-Spectroscopic Investigation of Selenium-Bearing Minerals from the Western US Phosphate Resource Area. *Geochem. Trans.* **2005**, *6* (1), 1–11.
- (29) Kang, M.; Ma, B.; Bardelli, F.; Chen, F.; Liu, C.; Zheng, Z.; Wu, S.; Charlet, L. Interaction of Aqueous Se(IV)/Se(VI) with FeSe/FeSe₂: Implication to Se Redox Process. *Journal of Hazardous Materials* **2013**, *248–249*, 20–28.
- (30) Charlet, L.; Kang, M.; Bardelli, F.; Kirsch, R.; Géhin, A.; Grenèche, J.-M.; Chen, F. Nanocomposite Pyrite–greigite Reactivity toward Se(IV)/Se(VI). *Environ. Sci. Technol.* **2012**, *46* (9), 4869–4876.
- (31) Kang, M.; Chen, F.; Wu, S.; Yang, Y.; Bruggeman, C.; Charlet, L. Effect of pH on Aqueous Se(IV) Reduction by Pyrite. *Environ. Sci. Technol.* **2011**, *45* (7), 2704–2710.
- (32) Jung, B.; Safan, A.; Batchelor, B.; Abdel-Wahab, A. Spectroscopic Study of Se (IV) Removal from Water by Reductive Precipitation Using Sulfide. *Chemosphere* **2016**, *163*, 351–358.
- (33) Curti, E.; Aimoz, L.; Kitamura, A. Selenium Uptake onto Natural Pyrite. *J. Radioanal. Nucl. Chem.* **2013**, *295* (3), 1655–1665.
- (34) Wei, D.; Osseo-Asare, K. Particulate Pyrite Formation by the Fe³⁺/H₂S - Reaction in Aqueous Solutions: Effects of Solution Composition. *Colloids Surf., A* **1996**, *11*.
- (35) Diener, A.; Neumann, T. Synthesis and Incorporation of selenide in Pyrite and mackinawite. *Radiochim. Acta* **2011**, *99* (12), 791–798.
- (36) Fortune, W. B.; Mellon, M. G. Determination of Iron with O-Phenanthroline: A Spectrophotometric Study. *Industrial & Engineering Chemistry Analytical Edition* **1938**, *10* (2), 60–64.
- (37) Cline, J. D. Spectrophotometric Determination of Hydrogen Sulfide in Natural Waters. *Limnology and Oceanography* **1969**, *14* (3), 454–458.
- (38) Doebelin, N.; Kleeberg, R. Profex: A Graphical User Interface for the Rietveld Refinement Program BGMN. *Journal of applied crystallography* **2015**, *48* (5), 1573–1580.
- (39) Scheinost, A.; Claussner, J.; Exner, J.; Feig, M.; Findeisen, S.; Hennig, C.; Kvashnina, K.; Naudet, D.; Prieur, D.; Rossberg, A.; Schmidt, M.; Qiu, C.; Colomp, P.; Cohen, C.; Dettona, E.; Dyadkin, V.; Stumpf, T. ROBL-II at ESRF: A Synchrotron Toolbox for Actinide Research. *Journal of Synchrotron Radiation* **2021**, *28*, 333–349.
- (40) Ravel, B.; Newville, M. ATHENA and ARTEMIS: Interactive Graphical Data Analysis Using IFEFFIT. *Phys. Scr.* **2005**, *2005* (T115), 1007.
- (41) Hafner, J.; Kresse, G. The Vienna AB-Initio Simulation Program VASP: An Efficient and Versatile Tool for Studying the Structural, Dynamic, and Electronic Properties of Materials; Springer **1997**. DOI: 10.1007/978-1-4615-5943-6_10.
- (42) Paier, J.; Hirschl, R.; Marsman, M.; Kresse, G. The Perdew–Burke–Ernzerhof Exchange–Correlation Functional Applied to the G2–1 Test Set Using a Plane-Wave Basis Set. *J. Chem. Phys.* **2005**, *122* (23), 234102.
- (43) Perdew, J. P.; Burke, K.; Ernzerhof, M. Generalized Gradient Approximation Made Simple. *Phys. Rev. Lett.* **1996**, *77* (18), 3865–3868.
- (44) Blöchl, P. E.; Jepsen, O.; Andersen, O. K. Improved Tetrahedron Method for Brillouin-Zone Integrations. *Phys. Rev. B* **1994**, *49* (23), 16223–16233.
- (45) Tang, W.; Sanville, E.; Henkelman, G. A Grid-Based Bader Analysis Algorithm without Lattice Bias. *J. Phys.: Condens. Matter* **2009**, *21* (8), No. 084204.
- (46) Sanville, E.; Kenny, S. D.; Smith, R.; Henkelman, G. Improved grid-based algorithm for Bader charge allocation. *J. Comput. Chem.* **2007**, *28* (5), 899–908.
- (47) Henkelman, G.; Arnaldsson, A.; Jónsson, H. A Fast and Robust Algorithm for Bader Decomposition of Charge Density. *Comput. Mater. Sci.* **2006**, *36* (3), 354–360.
- (48) Yu, M.; Trinkle, D. R. Accurate and Efficient Algorithm for Bader Charge Integration. *J. Chem. Phys.* **2011**, *134* (6), No. 064111.
- (49) Rieder, M.; Crelling, J. C.; Sustai, O.; Drábek, M.; Weiss, Z.; Klementová, M. Arsenic in Iron Disulfides in a Brown Coal from the North Bohemian Basin, Czech Republic. *International Journal of Coal Geology* **2007**, *71* (2), 115–121.
- (50) Matamoros-Veloza, A.; Peacock, C. L.; Benning, L. G. Selenium Speciation in Framboidal and euhedral Pyrites in Shales. *Environ. Sci. Technol.* **2014**, *48* (16), 8972–8979.
- (51) Hunger, S.; Benning, L. G. greigite: A True Intermediate on the Polysulfide Pathway to Pyrite. *Geochem. Trans.* **2007**, *8*, 1.
- (52) Wang, T.; Qian, T.; Zhao, D.; Liu, X.; Ding, Q. Immobilization of Perrhenate Using Synthetic Pyrite Particles: Effectiveness and Remobilization Potential. *Science of The Total Environment* **2020**, *725*, 138423.
- (53) Son, S.; Hyun, S. P.; Charlet, L.; Kwon, K. D. Thermodynamic Stability Reversal of Iron Sulfides at the Nanoscale: Insights into the Iron Sulfide Formation in Low-Temperature Aqueous Solution. *Geochim. Cosmochim. Acta* **2022**, *338*, 220–228.
- (54) Bonnissel-Gissinger, P.; Alnot, M.; Ehrhardt, J.-J.; Behra, P. Surface Oxidation of Pyrite as a Function of pH. *Environ. Sci. Technol.* **1998**, *32* (19), 2839–2845.
- (55) Weerasooriya, R.; Tobschall, H. J. Pyrite–Water Interactions: Effects of pH and pFe on Surface Charge. *Colloids Surf., A* **2005**, *264* (1–3), 68–74.
- (56) Borah, D.; Senapati, K. Adsorption of Cd(II) from Aqueous Solution onto Pyrite. *Fuel* **2006**, *85* (12–13), 1929–1934.
- (57) Yang, Z.; Kang, M.; Ma, B.; Xie, J.; Chen, F.; Charlet, L.; Liu, C. Inhibition of U(VI) Reduction by Synthetic and Natural Pyrite. *Environ. Sci. Technol.* **2014**, *48* (18), 10716–10724.
- (58) Essington, M. E. Estimation of the Standard Free Energy of Formation of Metal Arsenates, Selenates, and Selenites. *Soil Science Society of America Journal* **1988**, *52* (6), 1574–1579.
- (59) Séby, F.; Potin-Gautier, M.; Giffaut, E.; Borge, G.; Donard, O. F. X. A Critical Review of Thermodynamic Data for Selenium Species at 25°C. *Chem. Geol.* **2001**, *171* (3–4), 173–194.
- (60) Mitchell, K.; Couture, R.-M.; Johnson, T. M.; Mason, P. R. D.; Van Cappellen, P. Selenium sorption and Isotope Fractionation: Iron(III) Oxides versus Iron(II) Sulfides. *Chem. Geol.* **2013**, *342*, 21–28.
- (61) Rodríguez, D. M.; Mayordomo, N.; Schild, D.; Shams Aldin Azzam, S.; Brendler, V.; Müller, K.; Stumpf, T. Reductive Immobilization of ⁹⁹Tc(VII) by FeS₂: The Effect of marcasite. *Chemosphere* **2021**, *281*, 130904.
- (62) Charlet, L.; Scheinost, A. C.; Tournassat, C.; Grenèche, J. M.; Géhin, A.; Fernández-Martínez, A.; Coudert, S.; Tisserand, D.; Brendler, J. Electron Transfer at the Mineral/Water Interface: Selenium Reduction by Ferrous Iron Sorbed on Clay. *Geochim. Cosmochim. Acta* **2007**, *71* (23), 5731–5749.
- (63) Diener, A.; Neumann, T.; Kramar, U.; Schild, D. Structure of Selenium Incorporated in Pyrite and mackinawite as Determined by XAFS Analyses. *Journal of Contaminant Hydrology* **2012**, *133*, 30–39.
- (64) Poulain, A.; Fernandez-Martinez, A.; Grenèche, J. M.; Prieur, D.; Scheinost, A. C.; Menguy, N.; Bureau, S.; Magnin, V.; Findling,

N.; Drnec, J.; Martens, I.; Mirolo, M.; Charlet, L. Selenium Nanowire Formation by Reacting Selenate with Magnetite. *Environ. Sci. Technol.* **2022**, 14817.

(65) Das, S.; Lindsay, M. B. J.; Essilfie-Dughan, J.; Hendry, M. J. Dissolved Selenium(VI) Removal by Zero-Valent Iron under Oxic Conditions: Influence of Sulfate and Nitrate. *ACS Omega* **2017**, 2 (4), 1513–1522.

(66) Kipp, M. A.; Algeo, T. J.; Stüeken, E. E.; Buick, R. Basinal Hydrographic and Redox Controls on Selenium Enrichment and Isotopic Composition in Paleozoic Black Shales. *Geochim. Cosmochim. Acta* **2020**, 287, 229–250.